DC Voltage Control with Grid-forming Capability for Enhancing Stability of HVDC System

Ghazala Shafique, Johan Boukhenfouf, François Gruson, *Member*, *IEEE*, Frédéric Colas, *Member*, *IEEE*, and Xavier Guillaud, *Member*, *IEEE*

***Abstract*—Grid-forming (GFM) converters are recognized for their stabilizing effects in renewable energy systems. Integrating GFM converters into high-voltage direct current (HVDC) systems requires DC voltage control. However, there can be a conflict between GFM converter and DC voltage control when they are used in combination. This paper presents a rigorous control design for a GFM converter that connects the DC-link voltage to the power angle of the converter, thereby integrating DC voltage control with GFM capability. The proposed control is validated through small-signal and transient-stability analyses on a modular multilevel converter (MMC)-based HVDC system with a point-to-point (P2P) GFM-GFM configuration. The results demonstrate that employing a GFM-GFM configuration with the proposed control enhances the stability of the AC system to which it is connected. The system exhibits low sensitivity to grid strength and can sustain islanding conditions. The high stability limit of the system with varying grid strength using the proposed control is validated using a system with four voltage source converters.**

***Index Terms*—DC voltage control, grid-forming (GFM) converter, high-voltage direct current (HVDC), modular multilevel converter (MMC), stability analysis.**

I. Introduction

To mitigate the effects of climate change, a substantial shift towards the adoption of renewable energy sources has occurred. This shift has led to a considerable increase in the use of power electronic converters for integrating renewable energy sources into power transmission and distribution grids. The predominant method for managing these converters is the widely known and standardized grid-following (GFL) control, which relies on a phase-locked loop (PLL) for synchronization. However, an increase in GFL-controlled sources contributes to the destabilization of power grids, particularly due to their instability under weak grid conditions [1].

Recent advancements have highlighted grid-forming (GFM) control as a promising solution for addressing the stability challenges that hinder the widespread adoption of converter-interfaced resources. For example, the GFM control exhibits more stable behavior than the GFL control, particularly in weak AC grids [2]. The concept of GFM control is based on "voltage behind an impedance" behavior. The direct consequence is that the active power is not controlled by the current (as in GFL control), but by the voltage angle. An active power loop must be implemented to manage the power flow through the converter. Thus, this loop has two aims: to control the active power and synchronize the converter with the grid [3].

In a point-to-point (P2P) high-voltage direct current (HVDC) link with voltage source converters (VSCs), as shown in Fig. 1, the commonly used DC voltage control employs master-slave control, where the two stations play complementary roles. p_{ac} is the AC power; and other variables are defined in the following text. VSC 1 is responsible for the DC bus voltage control, whereas VSC 2 operates under power control mode, which controls the power flow. The dynamics of the DC-link voltage reflect the active power balance at the DC link, and the DC voltage control is crucial for maintaining the stability [4].

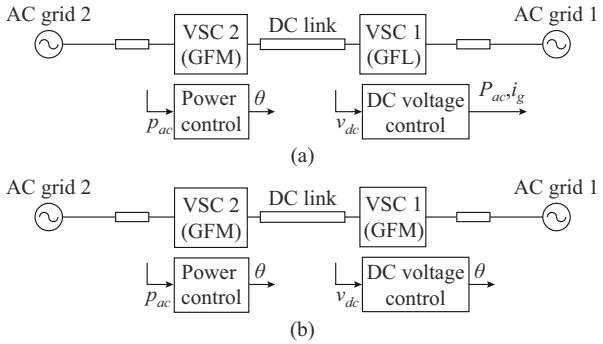

Fig. 1. P2P HVDC link with VSCs. (a) GFM-GFL configuration. (b) GFM-GFM configuration.

In addition, in a P2P HVDC link with GFM-GFL configuration, as illustrated in Fig. 1(a), one converter can operate under GFM control mode when connected to a very weak AC grid, whereas the other operates under GFL control mode when connected to a comparatively stronger AC grid.

Manuscript received: July 30, 2024; revised: October 26, 2024; accepted: December 24, 2024. Date of CrossCheck: December 24, 2024. Date of online publication: January 20, 2025.

This work was developed during the DICIT project sponsored by a public grant overseen by the French National Research Agency (No. ANR-20-CE05-0034 DICIT).

G. Shafique (corresponding author) and X. Guillaud are with Ecole Centrale de Lille, Laboratory of Electrical Engineering and Power Electronic (L2EP), Lille, France (e-mail: ghazala.shafique@ensam.eu; xavier.guillaud@centralelille.fr).

J. Boukhenfouf, F. Gruson, and F. Colas are with Arts et Métiers Institute of Technology, Laboratory of Electrical Engineering and Power Electronic (L2EP), Lille, France (e-mail: johan.boukhenfouf@ensam.eu; francois.gruson@ensam.eu; frederic.colas@ensam.eu).

DOI: 10.35833/MPCE.2024.000822

However, when the AC grids are weak on both sides of the P2P HVDC link, it is advantageous to operate both converters with GFM control for achieving a higher system stability [5]. In this situation, a GFM-GFM configuration is formed, as depicted in Fig. 1(b). For example, as given in [5], in the Caprivi link project, both converters operate in GFM control as both sides of the AC grids are extremely weak.

DC voltage control with GFL converters is well known in the literature [6], [7]. Therefore, in a GFM-GFL configuration, the GFL converter (VSC 1) would control the DC voltage, and a classical GFM control [8] can be implemented for the GFM converter (VSC 2). However, this problem would arise with a GFM-GFM configuration. Thus, the question that emerges for VSC 1 is whether it is possible to use the concept of GFM with DC voltage control.

The first method is to cascade an external DC bus voltage control loop into a classical GFM control [9]-[12]. In other words, the power reference is provided by the DC voltage controller, which is used by the power angle controller. However, this poses challenges because the GFM control of active power is often slow. Consequently, the DC voltage control response may be very slow, which potentially affects the DC voltage performance [13], [14]. In [15], DC voltage control is used, followed by power synchronization control, which allows both inertial support and DC voltage support via the same converter. However, the value of DC-link stored energy is not clear for a multi-terminal DC (MTDC) system. This method would work only when the value of energy storage is high, which would further increase the volume and cost of the converter.

The second method is to control the dynamics of the DC-link voltage directly using the converter angle, omitting the use of active power feedback control. Several studies have proposed solutions to this dynamic control issue. Reference [16] is among the first studies to propose a DC-link voltage control using the grid angle. Reference [17] proposes to apply the same type of control for a static synchronous compensator (STATCOM) application. References [18] and [19] improve the DC bus stability by adding a feedforward action to the control, and [20] analyzes the transient stability of this type of control. Compared with these previous works, this paper proposes a control design based on a pole placement method that allows control of the damping and response time of a closed system.

The control is applied to a modular multilevel converter (MMC)-based HVDC system with a GFM-GFM configuration to simulate a real application. Reference [21] presents the operation of an HVDC link with GFM-GFM configuration using a DC voltage control. However, it manages to achieve a stable system with only weak grids and is found to be unstable with strong grids, whereas the proposed control maintains stability for any type of grid.

These improvements can be considered extensions of previously proposed control methods. The main novelty of this paper lies in showing the significant advantages of employing this type of control for AC grids to which it is connected. Specifically, an enhancement to small-signal stability is demonstrated for an AC grid with a high penetration of power electronic converters, and the islanding capability provided by the proposed GFM control is significantly improved.

The remainder of this paper is organized as follows. Section II describes the development of the proposed control and validation through an electromagnetic transient (EMT) analysis of a P2P HVDC link with GFM-GFM configuration. Section III highlights the stability advantages of the P2P HVDC link with GFM-GFM configuration using the proposed control as compared with the GFM-GFL configuration using a classical DC voltage control. Section IV extends the findings for a more complex four-VSC system. Finally, conclusions are given in Section V.

II. Proposed Control and Validation Through EMT Analysis

This section proposes the DC voltage control while retaining the GFM capability of the converter. Time-domain validation of the proposed control is also conducted through EMT analysis.

A. System Model

To design a system that offers DC voltage control with GFM capabilities, it is first necessary to define a system model. Figure 2 shows a simplified system model with an AC grid, a DC grid, and a power converter, where i_{dc1} and i_{dc2} are the DC currents of the primary source and converter, respectively; v_{dc} is the DC bus voltage; C_{dc} is the DC bus capacitor; v_m^* is the modulated voltage; i_g is the grid current; v_g is the grid voltage; and X_c is the leakage reactance. The AC grid is represented by a Thevenin equivalent system consisting of voltage source v_e and grid reactance X_g.

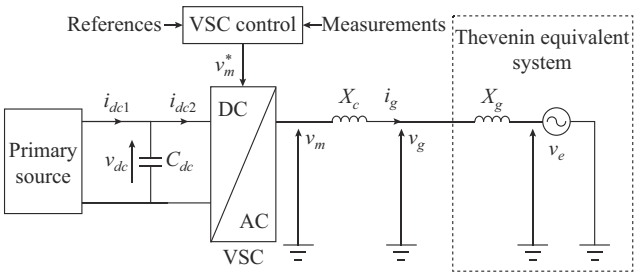

Fig. 2. Simplified system model.

1) Static Model of Converter for Power Synchronization Control

The primary role of the VSC is to modulate the DC bus voltage to produce a set of three-phase voltage v_m. Based on the average model, the converter can be approximated as an ideal three-phase voltage source, the values of which depend on the control system of the converter. The transformer is represented by a leakage reactance X_c, which maintains a lossless connection with the converter side.

In the steady state, each AC voltage V_x and current I_g can be expressed in phasor form (denoted by "$\overline{(\cdot)}$"):

$$\begin{cases} \overline{V}_x = V_x e^{j\delta_x} \\ \overline{I}_g = I_g e^{j(\delta_e - \phi)} \end{cases} \tag{1}$$

where V_x represents different voltages such as V_g, V_m, and

V_e, which are the steady-state values of v_g, v_m, and v_e, respectively; ϕ is the phasor angle between $\bar{I}_g$ and $\bar{V}_e$; and δ_x and δ_e are the corresponding phasor angles to the voltages V_x and V_e, respectively. In addition, the virtual inductance X_v is used to reduce the effects of phase shifts on power fluctuations in the converter [2]. A virtual voltage in phasor form $\bar{V}$ with a phasor angle δ is added to include the virtual inductance.

Thus, the system can be represented by the electrical circuit shown in Fig. 3(a) along with the corresponding phasor diagram in Fig. 3(b).

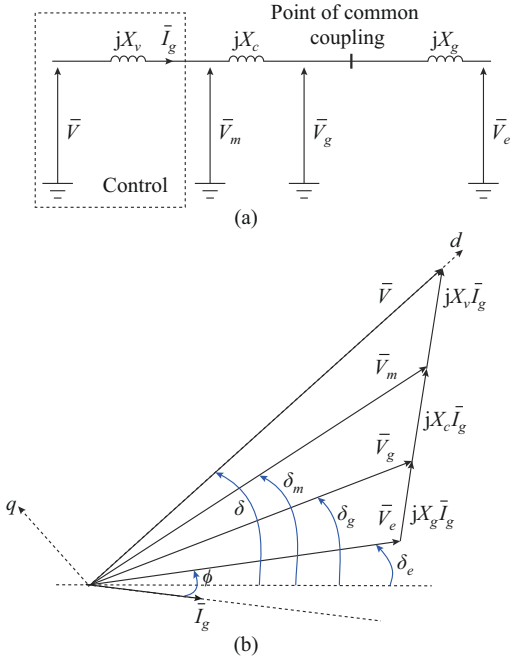

Fig. 3. Static model of converter that includes virtual inductance. (a) Electrical circuit. (b) Phasor diagram.

With this circuit, the active power P can be derived in terms of the phase angle as:

$$P=\frac{V_m V_e}{X_c+X_g}\sin(\delta_m-\delta_e) \tag{2}$$

where δ_m is the phasor angle of the voltage V_m.

From this, it can be deduced that active power control can be designed with different angles. In the time domain, each angle in the phasor corresponds to a time-varying angle θ_x as:

$$\theta_x=\delta_x+\omega_b t \tag{3}$$

where ω_b is the angular frequency.

Thus, δ_e and δ_m can be substituted with their corresponding time-domain angles θ_e and θ_m, respectively, and (2) can be rewritten as [2]:

$$P=\frac{V_m V_e}{X_c+X_g}\sin(\theta_m-\theta_e) \tag{4}$$

Including the virtual inductance, the active power P can be defined as:

$$P=\frac{VV_e}{X_v+X_c+X_g}\sin(\theta-\theta_e) \tag{5}$$

where V is the virtual voltage; and θ is the corresponding time-domain angle of δ.

As this angle difference is very small, (5) can be written as:

$$P\approx\frac{VV_e}{X_e}(\theta-\theta_e) \tag{6}$$

$$X_e=X_v+X_c+X_g \tag{7}$$

Thus, in the steady state, using (6), a block of the converter model in the frequency domain is obtained, as shown in Fig. 4(a).

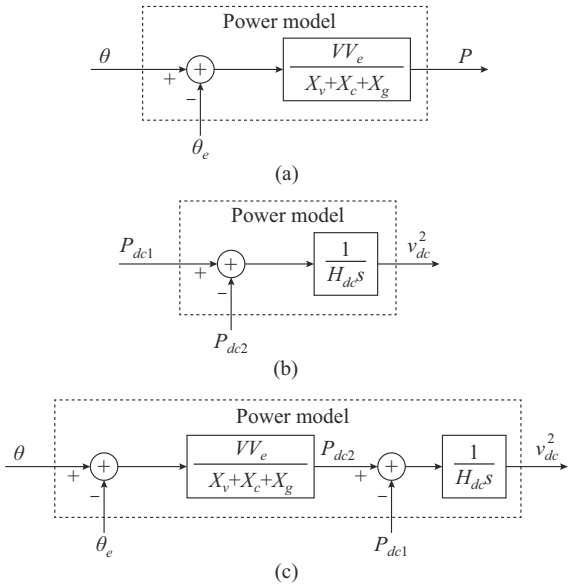

Fig. 4. Model representation in frequency domain. (a) Static model of converter. (b) Static model of DC link. (c) Combined system model.

2) Static Model of DC Link

For simplicity, the DC cable is represented by a capacitor. The dynamics of the capacitor are given by (8), as shown in Fig. 2. Here, C_{dc} is the total capacitance that includes the capacitance of the DC cable and capacitance related to the converter, namely the capacitance of the filter in the case of the VSC, or the virtual capacitance in the case of the MMC if virtual capacitance control is implemented [22]. By transforming this equation to obtain the power dynamics, the relationship between the DC voltage and DC power is given by (9). C_{dc} is expressed as the DC inertia H_{dc} in a per-unit system, as given in (10) [23].

$$i_{dc1}-i_{dc2}=\frac{1}{C_{dc}}\frac{\mathrm{d}v_{dc}}{\mathrm{d}t} \tag{8}$$

$$p_{dc1}-p_{dc2}=\frac{1}{H_{dc}}\frac{\mathrm{d}v_{dc}^2}{\mathrm{d}t} \tag{9}$$

$$H_{dc}=\frac{1}{2}C_{dc}\frac{v_{dc,ref}^2}{P_N} \tag{10}$$

where i_{dc1} and i_{dc2} are the DC currents of the primary source and converter, respectively; p_{dc1} is the DC power from the primary source; p_{dc2} is the DC power of the converter; and P_N and $v_{dc,ref}$ are the nominal power and DC voltage reference, respectively. Through (9), a block of the power dynam-

ics of the DC link in the frequency domain is presented in Fig. 4(b), where P_{dc1} and P_{dc2} are the steady-state values of p_{dc1} and p_{dc2}, respectively.

3) Combined System Model

Given that there are no losses in the converter, the AC active power is equal to the DC power of the converter. Thus, when the block diagrams in Fig. 4(a) and (b) are combined, the system can be represented by Fig. 4(c). It can be concluded that the DC voltage v_{dc} of the system can be controlled through the angle θ of the converter.

B. v_{dc}^2-θ Controller and Power Synchronization

Based on the system model as shown in Fig. 4(c), the controller between the DC voltage (v_{dc}^2) and the power angle of the converter (θ) is deduced as follows. An integrator must be added to the control to generate angle θ from frequency ω. This integral part of the control would result in a second-order system. Adding a derivative effect allows the addition of a second parameter to the controller and effective control of the dynamics of the second-order system.

The structure of the v_{dc}^2-θ controller is presented in Fig. 5, where K_p and K_d are the proportional and derivative gains of the controller, respectively; and $\tilde{\omega}_g$ is the estimated angular frequency. An angle reference θ^* is generated by the controller depending on the DC voltage deviation Δv_{dc}^2. This relationship can be derived from the structure presented in Fig. 5(a). Thus, θ^* is expressed as:

$$\begin{cases} \theta^* = \dfrac{\tilde{\omega}_g - \omega}{s}\omega_b \\ \omega = (K_p + K_d s)\Delta v_{dc}^2 \\ \Delta v_{dc}^2 = v_{dc,ref}^2 - v_{dc}^2 \end{cases} \tag{11}$$

As the real implementation of a derivative action can be sensitive to noise, a simple rearrangement of the control structure is performed to avoid the need for a derivative action of the signal. The modified structure of the v_{dc}^2-θ controller is shown in Fig. 5(b), which is transformed into two proportional actions. From the structure in Fig. 5(b), the relationship between the angle reference θ^* and the DC voltage deviation Δv_{dc}^2 is expressed as:

$$\theta^* = [(\tilde{\omega}_g - K_p \Delta v_{dc}^2)/s - K_d \Delta v_{dc}^2]\omega_b \tag{12}$$

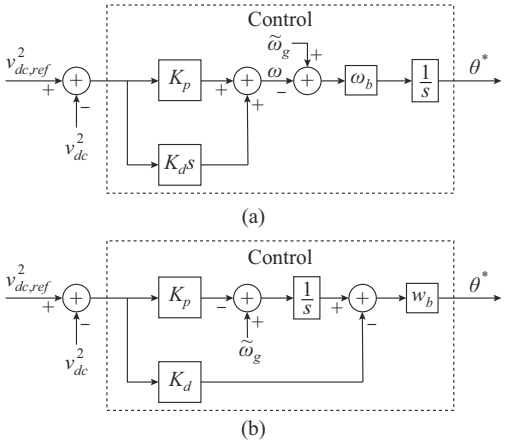

Fig. 5. Structure of v_{dc}^2-θ controller. (a) With derivative action. (b) With proportional action.

The combined system and control scheme is presented in Fig. 6, where the angle θ originates from the control reference angle θ^*. The resulting system is a second-order system. The transfer function between v_{dc}^2 and $v_{dc,ref}^2$ can be expressed as:

$$\frac{v_{dc}^2}{v_{dc,ref}^2} = \frac{1 + \dfrac{K_d}{K_p}s}{1 + \dfrac{K_d}{K_p}s + \dfrac{H_{dc}(X_v + X_c + X_g)}{K_p V V_e \omega_b}s^2} \tag{13}$$

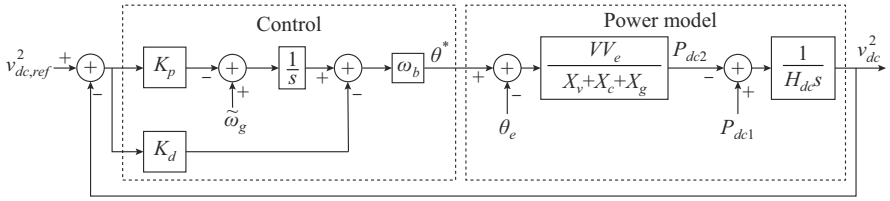

Fig. 6. Closed-loop DC voltage-power angle control.

The DC voltage control is achieved by controlling the angle of the converter. In addition, synchronization of the converter to the grid is achieved using the proposed control.

The generalized transfer function $f_T(s)$ of a second-order system without zeroes can be written as:

$$f_T(s) = \frac{1}{s^2 + 2\zeta\omega_n s + \omega_n^2} \tag{14}$$

where ω_n and ζ are the oscillation frequency and damping ratio, respectively.

The control parameters are designed using the pole placement method. As the resulting system (13) is a second-order system, the tuning of gains K_p and K_d is performed by comparing the transfer function with the generalized second-order transfer function (14) based on the chosen damping ratio and oscillation frequency. These values can be obtained by assuming the values of V and V_e to be approximate 1. In addition, the transfer function indicates the need for the grid impedance value. A strong grid is assumed to tune the controller by setting $X_g = 0$.

The next subsection analyzes the dynamics of the system using the proposed control through EMT analysis.

C. Time-domain Validation of Proposed Control

To validate the proposed control, EMT analysis is performed on a P2P HVDC link with GFM-GFM configuration, as shown in Fig. 1(b). The parameters are listed in Table I, where S_{nom} and S_b are the nominal and base apparent power,

respectively; P_{nom} is the nominal active power; $V_{dc,nom}$ is the nominal voltage of DC bus; and U_{nom} and U_b are the nominal and base phase-to-phase voltages on the AC grid side, respectively. The VSC 2 operates under constant power mode with voltage control grid-forming (VC-GFM) control [2], [24], providing inertial and damping effects denoted as H and ζ, respectively. VSC 1 controls the DC voltage with GFM capability.

TABLE I
PARAMETERS OF P2P HVDC LINK

Parameter	Value	Parameter	Value
S_{nom}, S_b	1.044 GVA, 1.044 GVA	U_{nom}, U_b	400 kV, 400 kV
P_{nom}	1 GW	$V_{dc,nom}$	640 kV
X_g	0.2 p.u.	X_{g2}	0.1 p.u.
X_v	0.15 p.u.	H_{dc}	100 ms

Accordingly, the proposed control is implemented using VSC 1. The parameters of the controller K_p and K_d are calculated to correspond to the desired time response t_r and damping ratio ζ. This system is studied for several disturbance events.

1) Case 1: Step on Power Reference at VSC 2 Converter Station

At $t=2$ s, a 0.5 p.u. step on the power reference is applied at the VSC 2 converter station. A time response of 100 ms is chosen for the v_{dc}^2-θ controller. The resulting DC voltage and power at both stations are presented in Fig. 7(a)-(c). Two scenarios are considered with different inertia values H for VC-GFM control of the VSC 2, i.e., $H=0.5$ s and $H=5$ s. The damping ratio is $\zeta=1$ in both scenarios. Given the power imbalance in the system, the DC voltage starts to decrease. As a result, the v_{dc}^2-θ controller operates to balance the power flow.

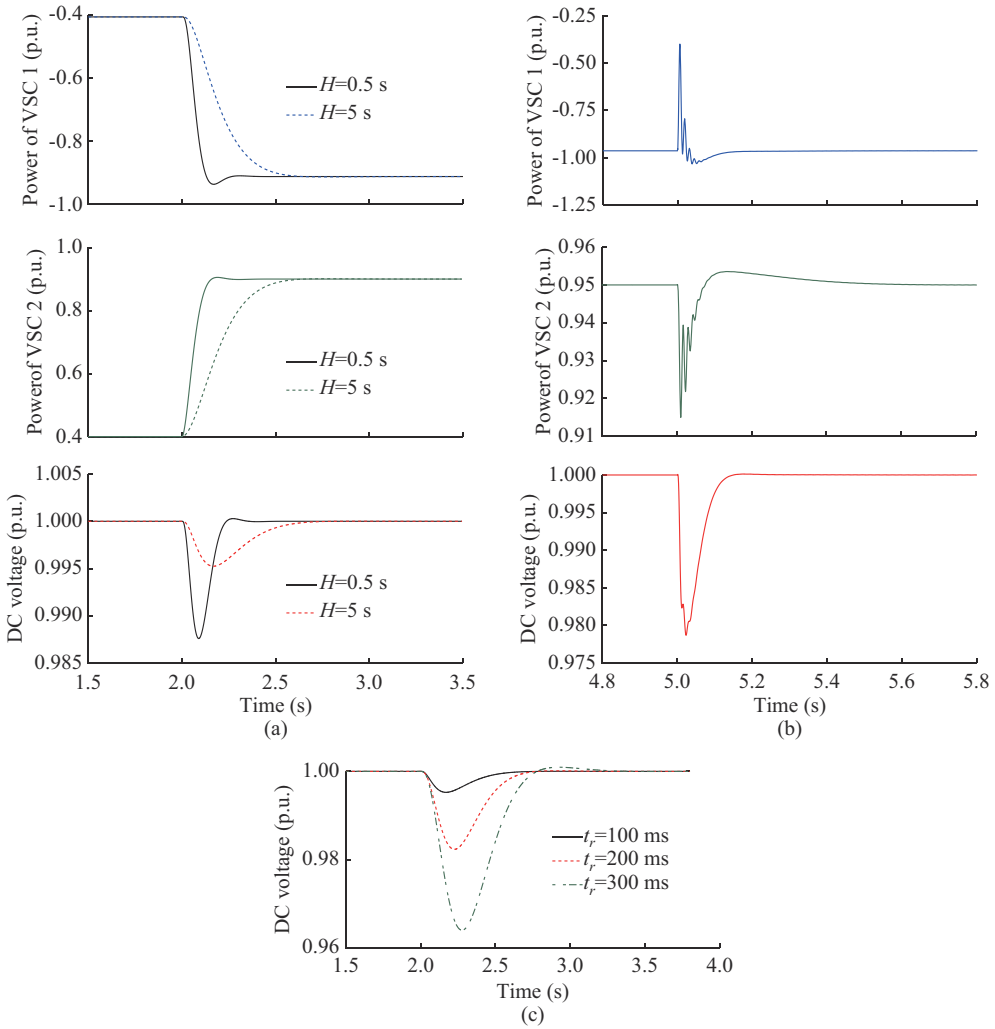

Fig. 7. Dynamic responses of P2P HVDC link after disturbances. (a) Case 1. (b) Case 2. (c) Case 3.

Figure 7 shows that the DC voltage is maintained at its reference value of 1 p.u.. For the scenario of $H=5$ s, the time response of the resulting power and DC voltage is approximately 300 ms. This is due to the high inertia value of the VSC 2. In addition, with a low inertia value ($H=0.5$ s) of the VSC 2 converter control, the response time of the DC voltage and power is approximately 100 ms.

2) Case 2: Phase Jump at AC Grid 1

In this case, a −10° phase jump is introduced at the voltage source of the Thevenin equivalent AC grid 1 at $t=5$ s. A

time response of 100 ms is chosen for the v_{dc}^2-θ controller, and the inertia value of $H=5$ s is chosen for VC-GFM control of the VSC 2. In Fig. 7(b), the resulting waveforms at VSC 1 and VSC 2 converter stations reveal that the system effectively restores synchronization. In addition, the DC voltage is maintained at the reference value in the steady state. The waveform follows the response according to the time response intended by the v_{dc}^2-θ controller.

3) Case 3: Under Different Time Response Values

In this case, the response of the DC voltage is compared with various response time of the v_{dc}^2-θ controller. The response time and their corresponding K_p and K_d values are given in Table II. At $t=2$ s, a power variation of 0.5 p.u. is introduced to the power reference of the VSC 2. The resulting DC voltage waveform is presented in Fig. 7(c). In all scenarios, given various values of K_p and K_d, the DC voltage is maintained at its reference value in the steady state. The main differences derive from the response time for returning to the nominal DC voltage level.

TABLE II
PARAMETERS OF v_{dc}^2-θ CONTROLLER IN CASE 3

t_r (ms)	ζ	K_p	K_d
100	1	0.2387	0.0095
200	1	0.0597	0.0048
300	1	0.0265	0.0032

4) Case 4: Comparison with Existing Controller

In this case, the behavior of the v_{dc}^2-θ controller is compared with that of an existing controller in the literature, wherein the DC grid voltage is controlled via the angle of the converter, referred to as the DC-link voltage synchronization control (DVSC) [19], [20]. The DVSC utilizes a proportional-integral (PI) controller, with the parameters detailed in [19]. A power step of 0.5 p.u. is introduced at the VSC 2, and the resulting waveforms are shown in Fig. 8. The behavior of the DC grid voltage is more damped under the v_{dc}^2-θ controller than under the DVSC controller. Thus, the v_{dc}^2-θ controller exhibits better damping and works well for both strong and weak grids. This is discussed in detail in the following section.

This validates the effectiveness of the proposed DC voltage control, which is successfully implemented in a P2P HVDC link with GFM-GFM configuration, achieving system stability without any conflicts with DC voltage control.

III. STABILITY ADVANTAGES OF P2P HVDC LINK WITH GFM-GFM CONFIGURATION USING PROPOSED CONTROL

This section describes the advantages of an HVDC with GFM-GFM configuration with the proposed control as compared with that of the GFM-GFL configuration under the classical master-slave control in terms of stability, grid strength, and system islanding.

A. System Description

The studied system is an MMC-based HVDC system, as shown in Fig. 9. An energy-based control is employed to control the energy stored in MMCs [25].

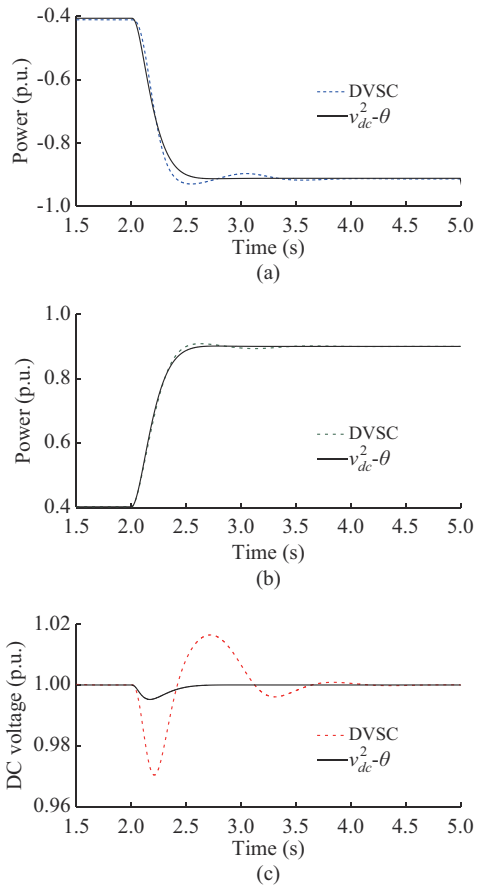

Fig. 8. Dynamic responses of P2P HVDC link after disturbances in Case 4. (a) Power of VSC 1. (b) Power of VSC 2. (c) DC voltage.

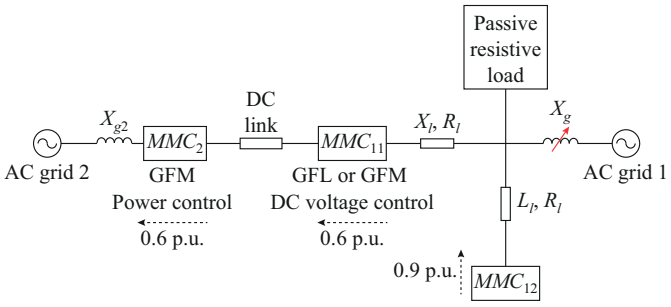

Fig. 9. Case study of MMC-based HVDC system.

The system includes two AC grid setups. On the AC grid 1 side, two MMCs are used, where MMC_{12} operates under GFL control mode, whereas MMC_{11} alternates between GFL and GFM control modes. Both MMCs are connected to the Thevenin equivalent via an overhead line. On the AC grid 2 side, MMC_2 operates in GFM control mode with VC-GFM control using the virtual synchronous machine (VSM) scheme [24]. MMC_{11} and MMC_2 are connected to a DC cable to form an HVDC system.

The DC link is modeled using a DC capacitor at $H_{dc}=100$ ms. The MMC-based HVDC system parameters are listed in Table III. More detailed MMC parameters are listed in Table IV.

The power flow is configured such that MMC_{12} injects power, which is absorbed by the passive load and MMC_{11} converter station.

TABLE III
MMC-BASED HVDC SYSTEM PARAMETERS

Component	Parameter	Value
MMC	S_{nom}, S_b	1.044 GVA, 1.044 GVA
	U_{nom}, U_b	400 kV, 400 kV
	P_{nom}	1 GW
	$V_{dc,nom}$	640 kV
Overhead line	Line impedance X_l	0.144 p.u.
	Line resistance R_l	0.0072 p.u.
Grid	X_{g2}	0.1 p.u.
	X_g/R_g	10
DC link	H_{dc}	100 ms
v_{dc}^2-θ controller	t_r	100 ms
	ζ	1
VC-GFM controller	H	5 s
	ζ	1

TABLE IV
MMC PARAMETERS

Parameter	Value
Arm inductance	0.18 p.u.
Arm resistance	0.005 p.u.
Connection impedance X_c	0.15 p.u.
Connection resistance R_c	0.005 p.u.
Virtual impedance X_v	0.06 p.u.
Energy in converter capacitance H_c	40 ms
Energy control parameters ω_n, ζ	3 Hz, 1
PLL parameters ω_n, ζ	50 Hz, 1

This arrangement limits the power flowing through the impedance of AC grid 1. The grid impedance can be increased with limited reactive power requirements, thereby rendering the system suitable for sensitivity analysis.

The grid strength is expressed by the grid impedance X_g. The test system is studied for different grid strengths on the AC grid 1 side by varying the grid inductance and resistance parameters L_g and R_g, while maintaining an X_g/R_g ratio of 10. The analysis is first performed through an EMT simulation in MATLAB, and then a small-signal analysis is conducted to determine the system stability limit.

B. Dynamic Behavior in the Case of a Strong Grid

The behavior of the system is next described, in which AC grid 1 is considered a strong grid with $X_g = 0.2$ p.u.. Two cases are analyzed. In one case, MMC_{11} operates in GFL control mode, and therefore, the P2P HVDC link has a GFM-GFL configuration. In the second case, MMC_{11} operates in GFM control mode with the v_{dc}^2-θ controller, creating a GFM-GFM configuration. Disturbances are introduced into the system, and the behavior of the system is analyzed in the two cases.

At $t = 2$ s, a power variation of 0.1 p.u. is applied at the MMC_2 converter station, and at $t = 4$ s, a phase jump of $\pi/18$ is introduced at AC grid 1. The resulting active power at each converter station and the DC voltage are obtained, as shown in Fig. 10. After a small transient, power flow is established in the steady state. Thus, in both cases, the MMC-based HVDC system is stable under a strong grid.

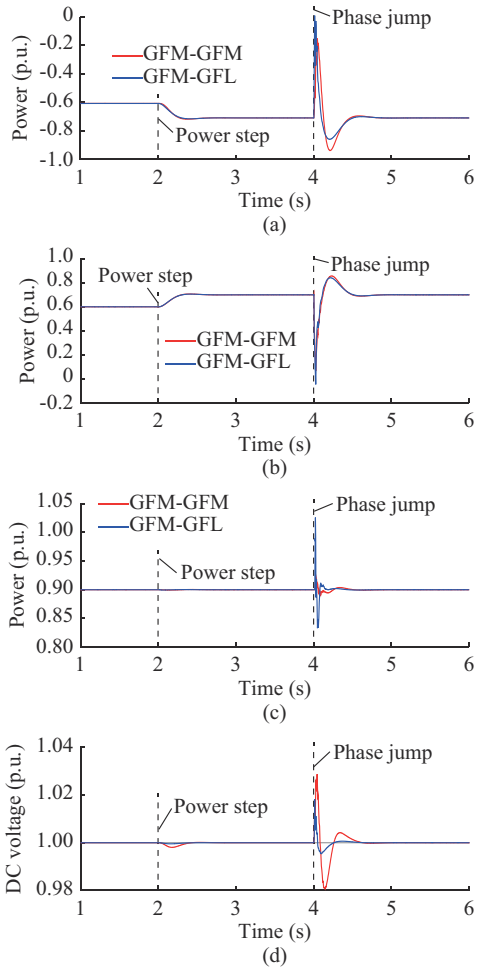

Fig. 10. Dynamic response in the case of a strong grid with $X_g = 0.2$ p.u.. (a) Power of MMC_{11}. (b) Power of MMC_2. (c) Power of MMC_{12}. (d) DC voltage.

C. Dynamic Behavior in the Case of a Weak Grid

Next, X_g is increased to 1 p.u. ($SCR = 1$) to consider AC grid 1 as a weak grid. When MMC_{11} operates in GFL control mode, the AC system becomes unstable, as shown in Fig. 11(a). The resulting power and DC voltage waveforms oscillate with a high magnitude. By contrast, when MMC_{11} operates in GFM control mode, the AC system maintains the stability. As Fig. 11(b) shows, the waveforms do not oscillate considerably, and their behavior is considerably damped.

Thus, as expected, utilizing a GFM-GFL configuration makes the system more sensitive to grid strength. By contrast, employing a GFM-GFM configuration with the proposed control enhances the stability of the system in terms of grid sensitivity.

To analyze the stability limit when employing the GFM-GFM and GFM-GFL configurations, a parametric sensitivity analysis is next performed under a small-signal stability analysis.

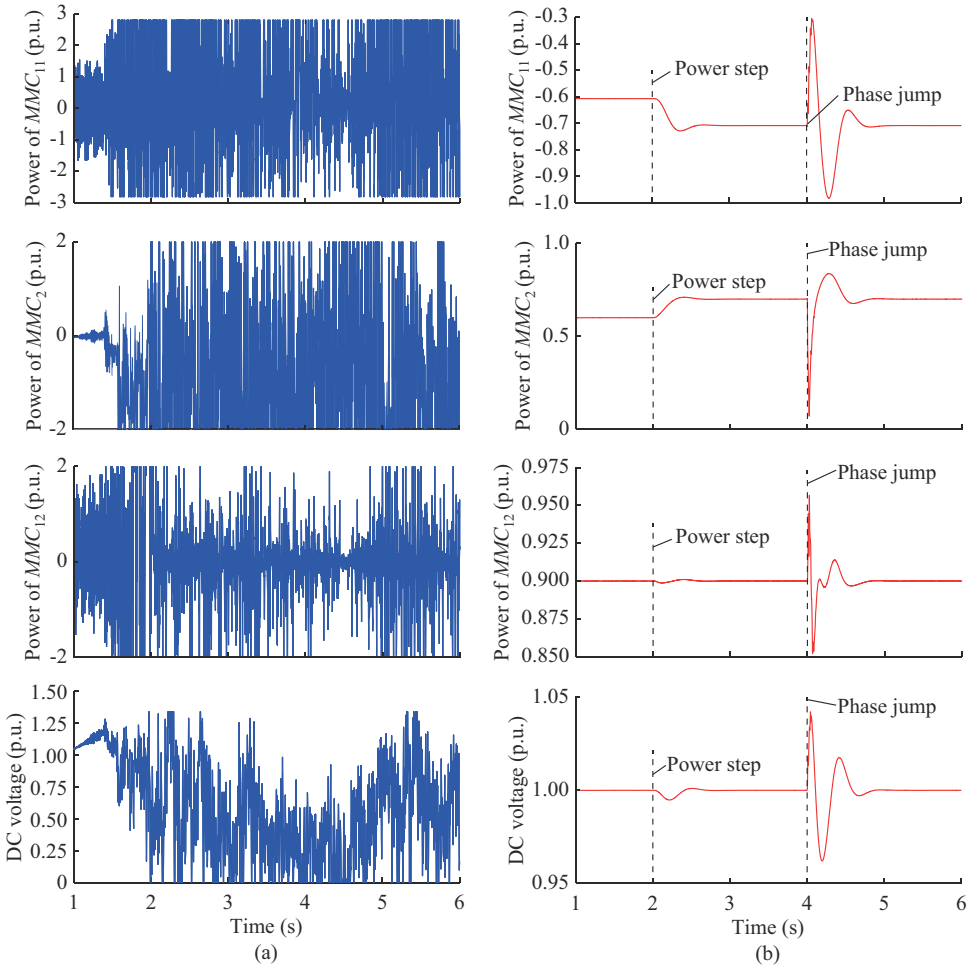

Fig. 11. Dynamic responses in the case of a weak grid with $X_g = 1$ p.u.. (a) MMC_{11} in GFL control mode. (b) MMC_{11} in GFM control mode.

D. Analysis of Stability Limit in Terms of Grid Strength

The small-signal stability limit is next examined for various grid strengths in the cases of GFM-GFL and GFM-GFM configurations.

To deepen the small-signal stability analysis of the system, a linearized state-space model is created. The state-space model of the system is developed by associating the state-space models of different subsystems, which are three MMCs, a DC cable, and two AC grids. The methodology presented in [26] is adopted to obtain a linearized model of the components.

The system is linearized around the same operating point, as shown in Fig. 9. Thus, a state-space model of the complete system is developed, linearized, and validated through EMT analysis.

The stability limit of the system is explored by varying the grid impedance parameter X_g, thereby varying the grid strength. The stability limit is recognized as the foremost operating point, where at least one eigenvalue of the linearized system exhibits a positive real part.

In the first case of the GFM-GFL configuration, the grid inductance X_g of the system varies from 0.2 to 3 p.u., and the resulting eigenvalue trajectories are obtained, as shown in Fig. 12. Beyond a certain threshold, the two eigenvalue pairs ($\lambda_{L1,L2}$ and $\lambda_{L3,L4}$) shift towards the right-hand side of the imaginary plane, leading to system instability. The stability limit for a GFM-GFL configuration is then obtained with $X_g = 0.5$ p.u.. For example, the participation factors of different states contributing to the eigenvalue $\lambda_{L3,L4}$ with $X_g = 1$ p.u. are presented in Fig. 13. Participation factor analysis reveals that the dominant states contributing to eigenvalues $\lambda_{L1,L2}$ and $\lambda_{L3,L4}$ are associated with the PLLs of MMC_{12} and MMC_{11}, as well as the AC current of MMC_{11} and the line current of AC grid 1, indicating an interaction between the converters through the AC grid. Thus, the instability due to the converter interaction increases.

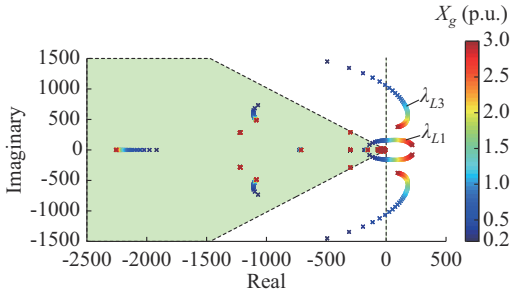

Fig. 12. Parametric sweep for change in grid strength X_g in the case of MMC_{11} with GFL control.

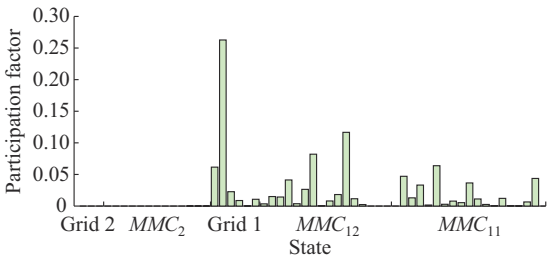

Fig. 13. Participation factors of different states contributing to eigenvalues $\lambda_{L3,L4}$ with $X_g=1$ p.u..

Next, the analysis of the stability limit of GFM-GFM configuration with the proposed control is conducted. The grid impedance X_g varies from 0.2 to 3 p.u., and the resulting eigenvalues are obtained, as shown in Fig. 14. The eigenvalues lie on the left-hand side of the plane for all values of X_g. Therefore, the system remains stable even with high values of X_g.

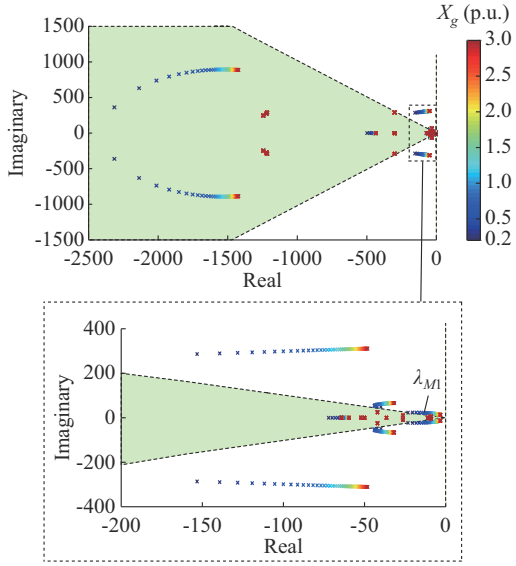

Fig. 14. Parametric sweep for change of grid strength X_g in the case of MMC_{11} with GFM control.

The participation factors of different states contributing to the most oscillatory pole/eigenvalue $\lambda_{M1,M2}$ with $X_g=1$ p. u. are presented in Fig. 15.

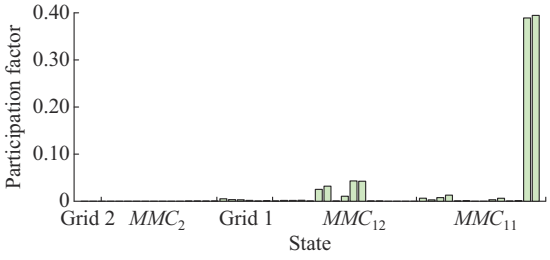

Fig. 15. Participation factors of different states contributing to the most oscillatory pole/eigenvalue $\lambda_{M1,M2}$ with $X_g=1$ p.u..

As observed, the dominant states are primarily associated with MMC_{11}, indicating less interaction between the converters and grids. In fact, the GFM-GFM setup with the proposed control exhibits minimal sensitivity to grid strength and represents a highly stable configuration.

E. Dynamic Behavior in the Case of Islanding with Loss of AC Grid 1

Thus far, the stability with respect to grid strength has been discussed. The stability of the system is next analyzed in the case of an islanding situation with loss of AC grid 1. Both AC grid impedances are low, i.e., $X_g=0.2$ p.u..

In the first case, MMC_{11} operates in GFL control mode. At $t=2$ s, a power disturbance of 0.05 p.u. is applied at the MMC_2 converter station. As a result, as shown in Fig. 16(a), the MMC_{11} converter station alters its power to compensate for the power variation and to return the DC voltage to its reference value. At $t=6$ s, a sudden loss occurs in AC grid 1. As indicated by the DC voltage and active power waveforms in Fig. 16(a), the system becomes unstable. Due to the absence of AC grid 1, the power flow is unbalanced and a sudden sizable drop in power and voltage occurs, followed by high oscillations in the system. Thus, the GFM-GFL configuration cannot sustain itself without an AC source.

In the second case, the MMC_{11} operates in GFM control mode, resulting in a GFM-GFM configuration with the proposed control. During the same islanding event at $t=6$ s, the behavior of the GFM control significantly differs from that of the GFL control. Due to the voltage source characteristics, the GFM control instantaneously adjusts its power to match the power required by the remaining AC grid 1. This leads to an imbalance in the DC bus power between the two stations, resulting in fast DC bus voltage variation. Once the DC voltage reaches its lower limit of 5%, the proposed control is shifted to the MMC_2 converter station [4], [27], and MMC_{11} operates in constant power mode. The DC voltage is recovered to its nominal value as soon as MMC_2 operates in DC voltage control mode.

Therefore, we can conclude that in the event of a large transient loss of an AC grid, the system is stable under the GFM-GFM configuration with the proposed control. Thus, the overall stability of the system is enhanced.

IV. Extension to a Four-VSC System

A. System Description

A four-VSC system is next introduced to demonstrate previous findings. A single-line diagram of the system is presented in Fig. 17, which consists of two wind parks (WPs), i. e., WP 1 and WP 2, and two HVDC links, i.e., HVDC 1 and HVDC 2.

WP 1 and WP 2 are consolidated representations of numerous generators and are GFL-controlled. HVDC 1 consists of two VSCs connected through a DC cable. VSC 2 is in GFM control mode, and VSC 1 is in GFM control mode with the proposed control or GFL control mode with classical master-slave control. However, the HVDC 2 is assumed to have a constant DC voltage with a GFL-controlled VSC.

The converter parameters are listed in Table V. The other detailed parameters can be found in [2].

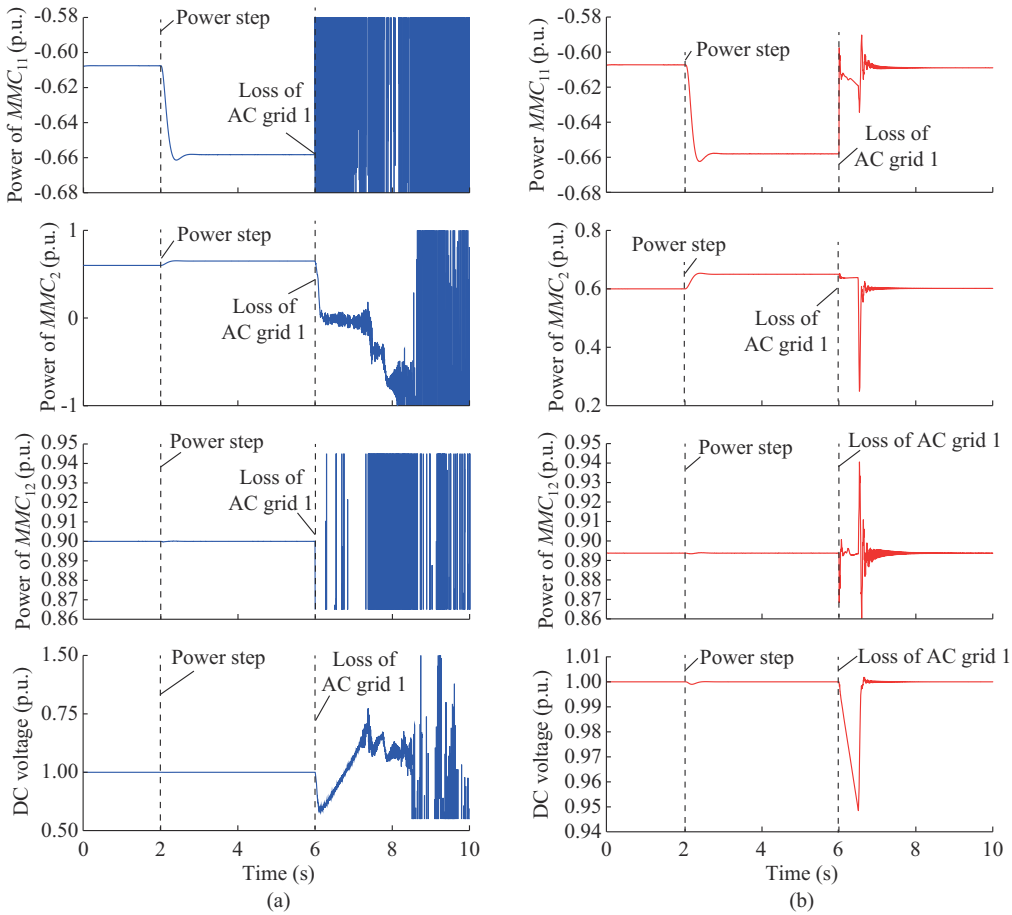

Fig. 16. Dynamic response in the case of loss of AC grid 1. (a) MMC_{11} in GFL control mode. (b) MMC_{11} in GFM control mode.

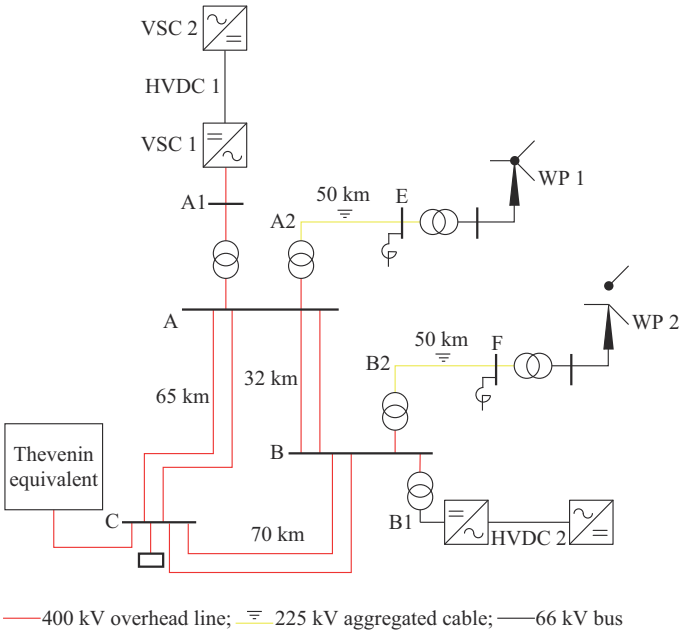

Fig. 17. Four-VSC system.

Both WPs are connected to the grid radially using six 225 kV cables of 50 km in length and six parallel transformers to handle the maximum output of each WP. The cables represent the AC connections of the offshore wind farms. The 400 kV segment of the transmission grid is interconnected in a meshed configuration, enhancing its reliability and flexibility. The system electrically incorporates multiple closely spaced VSCs to account for potential interactions.

TABLE V
CONVERTER PARAMETERS OF FOUR-VSC SYSTEM

Component	S_{nom} (MVA)	P_{nom} (MW)
WP 1	2400	2300
WP 2	2400	2300
HVDC 1	1200	1150
HVDC 2	1700	1630

The system is connected to an external grid via the Thevenin equivalent at bus C. The Thevenin voltage source stabilizes the system frequency to its nominal value under steady-state conditions. In addition, the strength of the external grid is adjustable in terms of short-circuit power.

B. Stability Enhancements with Proposed Control

The purpose of this paper is to examine and verify the stabilizing effects in GFM control mode with the proposed control. The system stability is evaluated based on the minimum short-circuit power of the external grid. The corresponding Thevenin reactance can be adjusted accordingly.

The operating points of the converters are listed in Table VI. Most of the power injected by the WPs is absorbed by the HVDC links, and the remaining power is taken by the load at bus C. Therefore, no power flows through the Thevenin equivalent. Therefore, the Thevenin reactance varies without concern about reaching the reactive power requirement limit.

When the short-circuit power from the external Thevenin equivalent at bus C is set to be 17.78 GVA, the system is found to be unstable when the VSC 1 is controlled in GFL control mode with the classical master-slave DC voltage control. This is demonstrated by applying a phase jump of $-\pi/40$ at the Thevenin equivalent voltage source. The resulting power at all the converter stations and the DC voltage of HVDC 1 are obtained, as shown in Fig. 18(a). It can be observed that the system becomes unstable with a small-signal disturbance.

TABLE VI
OPERATING POINTS OF CONVERTERS

Component	Injected power (MW)
WP 1	1500
WP 2	1500
HVDC 1	−1120
HVDC 2	−1600

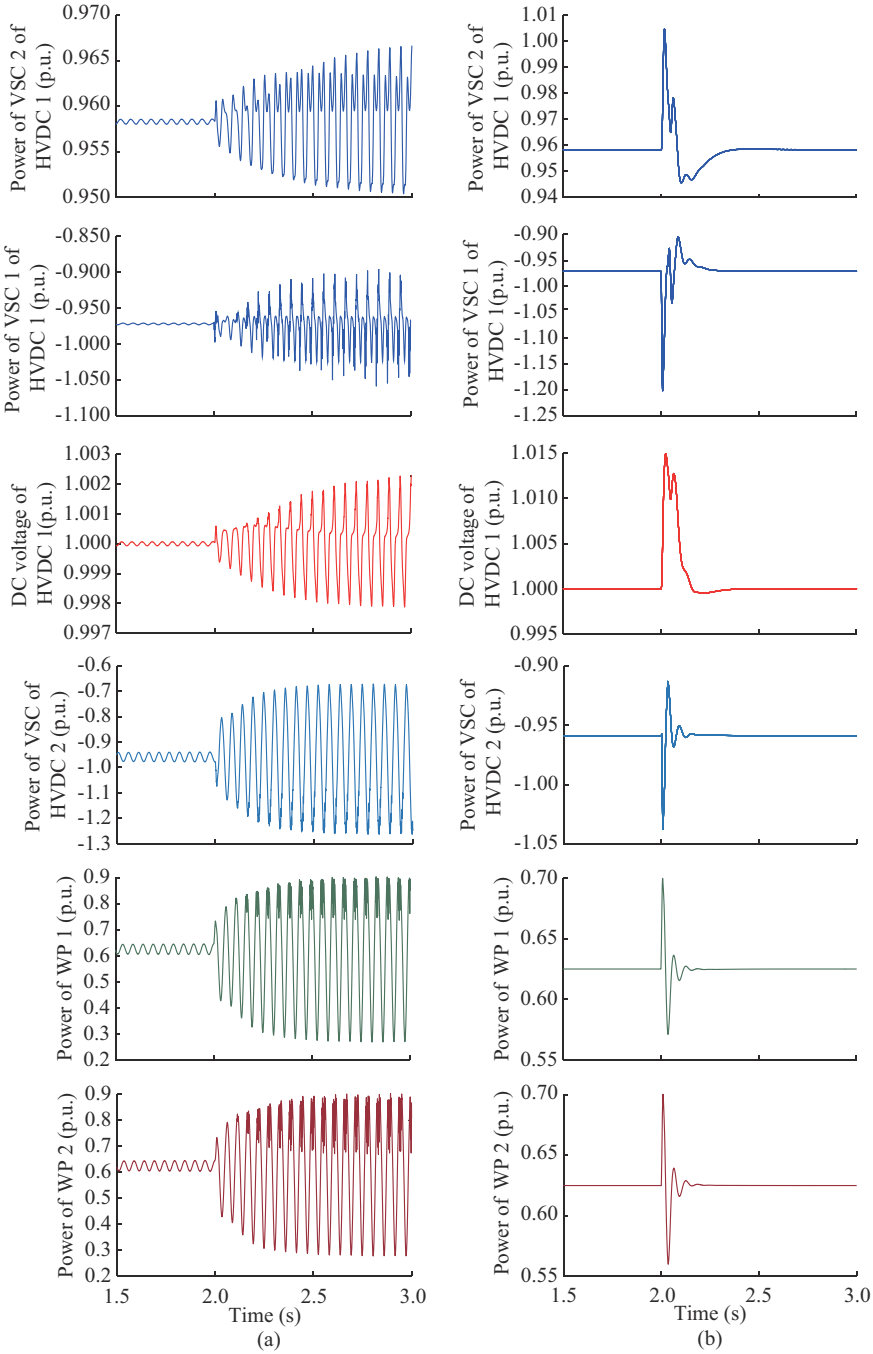

Fig. 18. Dynamic response of 4-VSC system after phase jump. (a) VSC 1 in GFL control mode. (b) VSC 1 in GFM control mode.

However, under the same conditions, the system remains stable when VSC 1 of HVDC 1 is controlled in GFM control mode with the v_{dc}^2-θ controller. As Fig. 18(b) shows, the DC voltage of HVDC 1 is maintained at its reference value at a steady state, and the power at all stations returns to its initial value after the phase jump.

This further confirms the previous findings regarding the stabilizing property of GFM control mode with the proposed control. Thus, an HVDC link with GFM-GFM configuration using the proposed control enhances the stability of the system and offers an overall more stable system.

V. Conclusion

This paper proposes a rigorous DC voltage control design for GFM converters and validates its performance in a P2P HVDC link with GFM-GFM configuration. The proposed control is an extension of the GFM principle. It has two aims: controlling the DC bus voltage and synchronizing the converter with the grid. Thus, both DC voltage control and GFM capabilities are provided. The stabilizing effects and additional benefits of the proposed control are demonstrated through a comparison of the GFM-GFM and GFL-GFM configurations under complex case studies. The results indicate that the GFM-GFM configuration with the proposed control achieves a higher stability limit in weak AC grids. In addition, an eigenvalue analysis highlights that the proposed control brings stability and avoids unwanted interactions between the converter and AC power system. Furthermore, the system remains stable in islanded scenarios with AC grid loss when using a GFM-controlled converter with the proposed control.

Further analysis is required to examine the behavior of the system under large disturbances such as multiple fault scenarios. Moreover, the proposed control for integrating the GFM control with DC voltage control is easily adaptable for MTDC systems. The proposed control can be extended to a master-slave MTDC system, where H_{dc} accounts for all the energy stored within the MTDC system. It is expected to enhance the overall stability of MTDC system to a significant degree but requires further investigation.

References

[1] A. Gole and J. Zhou, "VSC transmission limitations imposed by AC system strength and AC impedance characteristics," in *Proceedings of 10th IET International Conference on AC and DC Power Transmission (ACDC 2012)*, Birmingham, UK, Dec. 2012, pp. 1-6.

[2] C. Cardozo, T. Prevost, S.-H. Huang *et al.*, "Promises and challenges of grid forming: transmission system operator, manufacturer and academic view points," *Electric Power Systems Research*, vol. 235, p. 110855, Oct. 2024.

[3] X. Wang, M. G. Taul, H. Wu *et al.*, "Grid-synchronization stability of converter-based resources – an overview," *IEEE Open Journal of Industry Applications*, vol. 1, pp. 115-134, Aug. 2020.

[4] T. K. Vrana, J. Beerten, R. Belmans *et al.*, "A classification of DC node voltage control methods for HVDC grids," *Electric Power Systems Research*, vol. 103, pp. 137-144, Oct. 2013.

[5] Y. J. Hafner, A. Abdalrahman, M. Monge *et al.*, "Operating experiences and insights in future applications of grid forming capability of VSC HVDC," in *Proceedings of 2023 8th IEEE Workshop on the Electronic Grid (eGRID)*, Karlsruhe, Germany, Oct. 2023, pp. 1-8.

[6] S. S. Sayed and A. M. Massoud, "General classification and comprehensive performance assessment of multi-objective DC voltage control in multi-terminal HVDC networks," *IEEE Access*, vol. 9, pp. 34454-34474, Feb. 2021.

[7] P. Rault, "Dynamic modeling and control of multi-terminal HVDC grids," Ph.D. dissertation, Ecole Centrale de Lille, Lille, France, 2014.

[8] R. Rosso, X. Wang, M. Liserre *et al.*, "Grid-forming converters: control approaches, grid-synchronization, and future trends – a review," *IEEE Open Journal of Industry Applications*, vol. 2, pp. 93-109, Apr. 2021.

[9] L. Zhao, Z. Jin, and X. Wang, "Transient performance evaluation of grid-forming control for railway traction converters considering interphase operation," in *Proceedings of 2021 IEEE Energy Conversion Congress and Exposition (ECCE)*, Vancouver, Canada, Oct. 2021, pp. 2958-2963.

[10] J. Guo, Y. Chen, W. Wu *et al.*, "Wideband *dq*-frame impedance modeling of load-side virtual synchronous machine and its stability analysis in comparison with conventional PWM rectifier in weak grid," *IEEE Journal of Emerging and Selected Topics in Power Electronics*, vol. 9, pp. 2440-2451, Apr. 2021.

[11] L. Harnefors, M. Hinkkanen, U. Riaz *et al.*, "Robust analytic design of power-synchronization control," *IEEE Transactions on Industrial Electronics*, vol. 66, pp. 5810-5819, Aug. 2019.

[12] L. Zhang, L. Harnefors, and H.-P. Nee, "Power-synchronization control of grid-connected voltage-source converters," *IEEE Transactions on Power Systems*, vol. 25, pp. 809-820, May 2010.

[13] R. Wang, L. Chen, T. Zheng *et al.*, "VSG-based adaptive droop control for frequency and active power regulation in the MTDC system," *CSEE Journal of Power and Energy Systems*, vol. 3, no. 3, pp. 260-268, Oct. 2017.

[14] E. Rokrok, T. Qoria, A. Bruyere *et al.*, "Integration of a storage device to the DC bus of a grid-forming controlled HVDC interconnection," *Electric Power Systems Research*, vol. 212, p. 108601, Nov. 2022.

[15] A. E. Leon and J. M. Mauricio, "Virtual synchronous generator for VSC-HVDC stations with DC voltage control," *IEEE Transactions on Power Systems*, vol. 38, pp. 728-738, Jan. 2023.

[16] L. Huang, H. Xin, Z. Wang *et al.*, "A virtual synchronous control for voltage-source converters utilizing dynamics of DC-link capacitor to realize self-synchronization," *IEEE Journal of Emerging and Selected Topics in Power Electronics*, vol. 5, pp. 1565-1577, Dec. 2017.

[17] G. Li, F. Ma, Y. Wang *et al.*, "Design and operation analysis of virtual synchronous compensator," *IEEE Journal of Emerging and Selected Topics in Power Electronics*, vol. 8, pp. 3835-3845, Dec. 2020.

[18] L. Zhao, Z. Jin, and X. Wang, "Small-signal synchronization stability of grid-forming converters with regulated DC-link dynamics," *IEEE Transactions on Industrial Electronics*, vol. 70, pp. 12399-12409, Dec. 2023.

[19] L. Zhao, Z. Jin, and X. Wang, "Analysis and damping of low-frequency oscillation for DC-link voltage-synchronized VSCs," *IEEE Transactions on Power Electronics*, vol. 38, pp. 8177-8189, July 2023.

[20] L. Zhao, Z. Jin, and X. Wang, "Transient stability of grid-forming converters with flexible DC-link voltage control," in *Proceedings of 2022 International Power Electronics Conference*, Himeji, Japan, May 2022, pp. 1648-1653.

[21] X. Fan, Y. Chi, and Z. Wang, "Frequency support scheme of grid-forming based hybrid cascaded HVDC integrated wind farms," *IET Generation, Transmission & Distribution*, vol. 18, pp. 446-459, Feb. 2024.

[22] K. Shinoda, A. Benchaib, J. Dai *et al.*, "Virtual capacitor control: mitigation of DC voltage fluctuations in MMC-based HVDC systems," *IEEE Transactions on Power Delivery*, vol. 33, pp. 455-465, Feb. 2018.

[23] S. Samimi, "Modular multilevel converter model and control for the integration to the grid system," Ph.D. dissertation, Ecole Centrale de Lille, Lille, France, 2016.

[24] T. Qoria, "Grid-forming control to achieve a 100% power electronics interfaced power transmission systems," Ph.D. dissertation, Ecole Nationale Supérieure d'Arts et Métiers, Lille, France, 2020.

[25] S. Samimi, F. Gruson, P. Delarue *et al.*, "MMC stored energy participation to the DC bus voltage control in an HVDC link," *IEEE Transactions on Power Delivery*, vol. 31, pp. 1710-1718, Aug. 2016.

[26] J. Freytes, S. Akkari, J. Dai *et al.*, "Small-signal state-space modeling of an HVDC link with modular multilevel converters," in *Proceddigns of 2016 IEEE 17th Workshop on Control and Modeling for Power Electronics (COMPEL)*, Trondheim, Norway, Jun. 2016, pp. 1-8.

[27] CIGRE, "Control methodologies for direct voltage and power flow an

a meshed HVDC grid," Tech. Rep., CIGRE WG B4.58, 2017.

Ghazala Shafique received the master's degree from the University of Lille, Lille, France, in 2021, the Ph.D. degree at Ecole Nationale Supérieure d'Arts et Métiers, Lille, France, in 2024, and is currently working as a Researcher at Ecole Centrale de Lille, Laboratory of Electrical Engineering and Power Electronic (L2EP), Lille, France. Her research interests include high-voltage direct current (HVDC) transmission, power system control, and integration of power electronic converters into power systems.

Johan Boukhenfouf received the Engineering degree from Ecole Centrale de Lille, Lille, France, and Electrical Engineering degree from the University of Chile, Santiago, Chile, in 2021. He is currently working toward the Ph.D. degree at Arts et Métiers Institute of Technology, Laboratory of Electrical Engineering and Power Electronic (L2EP), Lille, France. His research interests include high-voltage DC-DC converter, DC transmision, and power electronic converter control.

François Gruson received the Ph. D. degree in electrical engineering from Ecole Centrale de Lille, Lille, in 2010. Since 2011, he has been working as Associate Professor at Arts and Metiers Arts et Métiers Institute of Technology, Laboratory of Electrical Engineering and Power Electronic (L2EP), Lille, France, where he received the accreditation to direct research (HDR) in 2022. His research interests include power electronic converter and power quality for applications in distribution and transmission systems, especially HVDC transmission system.

Frédéric Colas received the Ph. D. degree in control system from Ecole Centrale de Lille, Lille, France, in 2007. He is a Research Engineer at Arts et Métiers Institute of Technology, Laboratory of Electrical Engineering and Power Electronic (L2EP), Lille, France. His research interests include integration of renewable energy sources, advanced control technique for power systems, integration of power electronic converters, and real-time simulation for power system applications.

Xavier Guillaud received the Ph. D from University of Lille, Lille, France, in 1992, and joined the Laboratory of Electrical Engineering and Power Electronic (L2EP), Lille, France, in 1993. He has been a Professor in Ecole Centrale de Lille, Lille, France, since 2002. His current research interest includes integration of high-voltage power electronic converters in transmission system.